Meso-scale modelling of complex fibre composite geometries using an immersed boundary method

Downloaded from: https://research.chalmers.se, 2026-10-16 01:58 UTC

Citation for the original published paper (version of record):

Börjesson, E., Verhoosel, C., Remmers, J. et al (2024). Meso-scale modelling of complex fibre composite geometries using an immersed boundary method. Finite Elements in Analysis and Design, 242. http://dx.doi.org/10.1016/j.finel.2024.104262

N.B. When citing this work, cite the original published paper.

research.chalmers.se offers the possibility of retrieving research publications produced at Chalmers University of Technology. It covers all kind of research output: articles, dissertations, conference papers, reports etc. since 2004. research.chalmers.se is administrated and maintained by Chalmers Library

(article starts on next page)

Finite Elements in Analysis and Design 242 (2024) 104262

Contents lists available at ScienceDirect

Finite Elements in Analysis & Design

journal homepage: www.elsevier.com/locate/finel

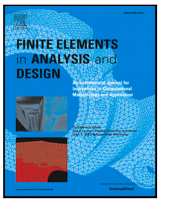

Meso-scale modelling of complex fibre composite geometries using an immersed boundary method

Elias Börjesson [a,*], Clemens V. Verhoosel [b], Joris J.C. Remmers [b], Martin Fagerström [a]

[a] Dept. Industrial and Materials Science, Chalmers University of Technology, Gothenburg, Sweden
[b] Dept. Mechanical Engineering, Eindhoven University of Technology, Eindhoven, The Netherlands

ARTICLE INFO

Keywords:
Meso-scale modelling
Immersed boundary methods
Finite Cell Method
Fibre composites

ABSTRACT

This paper investigates the application of immersed methods to simplify the discretisation and modelling process for meso-scale geometries in fibre-reinforced composites. The geometry of meso-scale structures in fibre-reinforced composites can often be categorised as complex, and frequently presents considerable challenges for meshing software. This complexity necessitates either time-consuming manual intervention or the adoption of simplified discretisation approaches, such as voxel methods, which may compromise accuracy. To address this issue, we study the use of immersed boundary methods, in combination with B-splines, for the discretisation of the matrix regions of the meso-scale geometry. This combination has the potential to minimise the requirement for manual intervention in the discretisation processes with little effect to the accuracy of e.g. stresses. We validate the proposed modelling framework in three numerical examples, where homogenised stiffnesses and stress levels are analysed in various fibre composite architectures.

1. Introduction

Fibre-reinforced composites provide an opportunity to significantly reduce structural weight, which can be advantageous in a range of industries such as marine, automotive, aerospace and sport technology. The competitive specific properties of fibre composites have sparked substantial interest in both academia and industry to develop new fibre composite materials, including high-performance thin-ply composites [1], damage-tolerant 3D-woven composites [2], and eco-friendly bio-composites [3]. Each of these composite variants carries distinct advantages and disadvantages, and it is essential to characterise and evaluate their performance for optimal design.

The performance of composite materials is significantly influenced by sub-scale features, both the separate material constituent and the reinforcement architecture. An effective approach to assess the behaviour of different sub-scale architectures, without the need for extensive physical testing, is to utilise meso-scale modelling approaches [4]. Here, the individual constituents and their geometry are explicitly accounted for, which facilitates the possibility to estimate effective material properties [5], monitor stresses and strains [6], and, in advanced cases, modelling of damage mechanisms and evolution [7].

Modelling the sub-scale of fibre composite materials is however not straightforward, and a multitude of open challenges exist. Following the road-map presented by Lomov et al. [4], multiple important stages are outlined in order for successful multi-scale modelling of fibre composites. One of the stages relates model generation and discretisation, where, we in our current contribution, focus on the efficient generation of the computational discretisation of the meso-scale model.

* Corresponding author.
E-mail address: elias.borjesson@chalmers.se (E. Börjesson).

https://doi.org/10.1016/j.finel.2024.104262
Received 8 May 2024; Received in revised form 30 August 2024; Accepted 9 September 2024
Available online 26 September 2024
0168-874X/© 2024 The Authors. Published by Elsevier B.V. This is an open access article under the CC BY license (http://creativecommons.org/licenses/by/4.0/).

As a basis for the discretisation, it is important to have an accurate description of the geometry of the underlying fibre architecture. Here, a large amount of alternatives for generating such geometries have been proposed, see e.g. Texgen [8] and WiseTex [9] for generation of idealised 3D or 2D woven geometries, the work by Wintiba et al. [10] or Stig et al. [11] for generation of 3D woven composites, the generation of woven bundle architecture via process simulation using the digital-chain method [12,13], or [14] for segmentation of CT-scans of real meso-scale structures.

Regardless of the method employed to generate meso-scale geometry, the generated geometry can often be classified as "complex". Irrespective of their architecture, fibre bundles are typically closely situated, leading to small gaps and sharp angles between them. These geometric features pose significant challenges during the meshing software, particularly in pure matrix regions, which can result in an extreme amount of elements, poor-quality elements or situations where the mesh generator not being able to generate a mesh at all. As a result, unwanted time-intensive manual interventions are therefore needed to obtain desirable models.

Given the challenges associated with creating standard finite element meshes for meso-scale models, many researchers have investigated new methods for automating the discretisation process. In recent years, significant progress has been made for the automatic generation of tetrahedral meshes. In Wintiba et al. [10], tetrahedral meshes were generated for complex 3D-woven composites using mesh generation techniques outlined in [15]. The quality of the elements are reasonably good, but many elements are generated between bundle interfaces and at sharp features. In Li et al. [16], the issue with the large amount of elements is addressed. Here, the narrow gaps and sharp features between bundles are removed by use of local modification of the bundle geometries, and bundles are directly connected with interface elements. This significantly reduces the number of elements in the model, in many cases as such as by a factor of 100.

Nevertheless, in many instances the generation of tetrahedral meshes is not feasible without extensive user intervention. This is evident by the multitude of alternative discretisation strategies used to circumvent standard boundary-fitted FE-meshes. One common alternative approach, extensively used in the literature, is voxel-based meshes [17–20]. The attractiveness of voxel-based meshes comes from the advantage in automated mesh generation, whereby labour-intensive manual meshing procedures are circumvented. Voxel meshes have been used to effectively estimate elastic stiffness properties [21], but may also be applicable in non-linear simulations [20,22]. However, due to the step-like nature of voxel meshes, a number of issues arise. First, a substantial number of elements are typically needed to adequately capture the relevant geometric features. Moreover, voxel meshes are unsuitable for interface-problems, since the surface area is inaccurately described (even with mesh-refinement). Finally, the step-like nature of voxel meshes also tends to generate artificial stress concentrations, when compared with standard meshes [23].

An approach that has gained a lot of attention for its ability to streamline the discretisation process for complex geometries is immersed boundary methods. There are many flavours of immersed methods, but the Finite Cell Method (FCM) [24], CutFEM [25] and the Embedded Element Method (EMM) [26] are three common options. The core idea of immersed methods is to use simple un-fitted (Cartesian) meshes to discretise the unknown fields, while the geometry is accurately captured with specially generated quadrature rules. Immersed methods have been an active research field for several decades, and have therefore been applied successfully in e.g. solid and fluid mechanics problems [27,28]. The main benefit of immersed methods is that the discretisation (or meshing) procedure can be automated, even for very complex geometries. A challenging aspect in immersed methods is the requirement to generate specialised quadrature schemes for the elements in the immersed mesh, as these elements generally do not conform to the physical domain of the problem.

An approach that is based on the principles of immersed boundary methods, specifically developed to simplify the discretisation procedure for meso-scale fibre composites, is the Independent Mesh Method (IMM) [29] (which has been independently developed from FCM). One of the core ideas is to mesh each meso-scale bundle independently. This has the benefit of significantly simplifying the meshing procedure for the bundles, as they are not constrained by the need to account for adjacent bundles or matrix regions. The pure matrix regions are in turn automatically discretised with the principles from immersed approaches, thereby circumventing a lot of manual meshing interventions. Moreover, the separate bundle and matrix meshes are coupled via penalty-constraints. The IMM has been shown to produce accurate results in linear elastic analyses as well as in large non-linear analyses of woven composites in [29,30].

In the current contribution, we propose to use the key aspects of IMM and leverage advancements from FCM to enhance the mesh discretisation process of meso-scale models of fibre composites. In alignment with IMM, we independently mesh each fibre bundles to significantly simplifying the meshing procedure for the individual bundles. For the pure matrix regions, we utilise the FCM method. Specifically, we explore ghost penalty stabilisation techniques developed for immersed boundary methods method. Moreover, we utilise B-splines basis functions to discretise the matrix regions. B-splines allow for higher-order continuity in between elements, which, compared to traditional Lagrange finite elements, provides a high-order piece-wise polynomial basis at fewer degrees of freedom. Especially when approximating sufficiently smooth solutions, this high-order continuity makes B-splines efficient in terms of the balance between accuracy and degrees of freedom. See e.g. [24,31,32] for successful applications. We note that the proposed framework is not restricted to B-spline basis functions and that alternative choices for the basis functions (e.g. spectral methods) may also perform well. To connect the independently discretised regions, we employ penalty constraints between the matrix and bundle phases.

The key contribution of this paper is to use the advancements within FCM, and investigate its applicability to meso-scale modelling of fibre reinforced composite materials. In particular,

- we demonstrate that stabilisation, in this case ghost penalty stabilisation, is important for robustness e.g. in preventing stress peaks in the resulting stress field,

- we evaluate how the density of the background discretisation, and the (adaptive) quadrature rule for the elements in the FCM mesh, affect the stress prediction in critical regions,
- we demonstrate that the proposed FCM modelling approach is well-suited to predict the bending and membrane stiffness in a composite with 3D-woven reinforcements, and
- we illustrate how FCM allows for an efficient parameter study to evaluate how the stress distribution in a thin-ply woven composite varies with varying bundle thicknesses.

The paper is organised as follows. In Section 2, we introduce the general framework, highlighting crucial aspects of the FCM method. This includes the integration of elements and how stabilisation techniques are employed to enhance the robustness of the model. In Section 3, we demonstrate the results through three numerical examples. The first example considers a two-dimensional textile composite RVE and illustrates the main techniques and features outlined in this paper. In the second and third numerical examples, the proposed framework is applied to realistic three-dimensional problems.

2. Immersed modelling framework for fibre composite meso-scale models

To explain the immersed modelling framework, we consider a standard setup of a fibre composite meso-scale problem, as shown in Fig. 1. The problem includes a computational domain $\Omega_\square$ with N_r fibre reinforcements bundles, each denoted $\Omega_r^i, i = 1, \dots, N_r$, and where the union of all reinforcements is denoted Ω_r. Note that depending on the type of composite and scale of interest, the reinforcements Ω_r can be individual fibres, fibre bundles or even discontinuous tape reinforcements. However, since all applications in the result section are concerning textile composites, we choose the meso-scale as the representative scale of interest, with impregnated fibre bundles being the corresponding reinforcement type. Moreover, the (possible) interfaces between bundles Ω_r^i and Ω_r^j are denoted Γ_r^{ij}. The bundles are set within a matrix domain Ω_m. Here, it assumed that the geometric parametrisation of the Ω_r is known, which leads to that the matrix domain is implicitly obtained as $\Omega_m = \Omega_\square - \Omega_r$. Finally, the interface between the matrix and bundles is denoted Γ_{rm}. Considering static equilibrium without the consideration of body forces, the strong form of the problem reads:

$$\nabla \cdot \boldsymbol{\sigma} = 0 \quad \text{in } \Omega_\square, \tag{1a}$$

$$[\![\boldsymbol{u}]\!] = \mathbf{0} \quad \text{on } \Gamma_r^{ij} \text{ and } \Gamma_{\text{rm}}, \tag{1b}$$

$$[\![\boldsymbol{t}]\!] = \mathbf{0} \quad \text{on } \Gamma_r^{ij} \text{ and } \Gamma_{\text{rm}}, \tag{1c}$$

$$[\![\boldsymbol{u}]\!]_\square = \bar{\boldsymbol{\varepsilon}} \cdot (\boldsymbol{x} - \bar{\boldsymbol{x}}) \quad \text{on } \Gamma_\square^+, \tag{1d}$$

where $\boldsymbol{u}$ is the unknown displacement field, $\boldsymbol{\sigma}(\boldsymbol{\varepsilon}(\boldsymbol{u}))$ is the Cauchy stress tensor, $\boldsymbol{t}$ is the traction vector on some surface, and $\bar{\boldsymbol{x}}$ is the centroid of $\Omega_\square$. Moreover, we will in this contribution only consider elastic small strains, $\boldsymbol{\varepsilon}(\boldsymbol{u}) = (\boldsymbol{u} \otimes \nabla)^{\text{sym}}$. Eqs. (1b) and (1c) enforces traction and displacement continuity across interfaces, where the jump across discontinuous interfaces is defined as $[\![\bullet]\!] = (\bullet^+ - \bullet^-)$, at some interface Γ. Eq. (1d) enforces periodic displacement boundary conditions on the external boundary of $\Omega_\square$, corresponding to an applied macroscale strain $\bar{\boldsymbol{\varepsilon}}$. In this regard, we have the displacement jump $[\![\boldsymbol{u}]\!]_\square$ defined as $[\![\boldsymbol{u}]\!]_\square = \boldsymbol{u}(\boldsymbol{x}^+) - \boldsymbol{u}(\boldsymbol{x}^-)$, were $\boldsymbol{x}^+$ is a point on $\Gamma_\square^+$ and $\boldsymbol{x}^-$ is the corresponding point on $\Gamma_\square^-$ (see Fig. 1). Note that also Dirichlet or Neumann boundary conditions are possible in Eq. (1d).

The corresponding weak form of the problem can be stated as, find $\boldsymbol{u}_h$ in V_h such that:

$$\int_{\Omega_\square} \boldsymbol{\sigma}(\boldsymbol{\varepsilon}(\boldsymbol{u}_h)) : \boldsymbol{\varepsilon}(\delta \boldsymbol{v}_h) \, \mathrm{d}\Omega + a_h^r(\boldsymbol{u}_h, \boldsymbol{v}_h) + a_h^{rm}(\boldsymbol{u}_h, \boldsymbol{v}_h) = 0 \quad \forall \boldsymbol{v}_h \in V_h^0, \tag{2}$$

where V_h and V_h^0 are sufficiently smooth spaces and satisfy the periodic boundary conditions. Moreover, $a_h^r(\boldsymbol{u}_h, \boldsymbol{v}_h)$ and $a_h^{rm}(\boldsymbol{u}_h, \boldsymbol{v}_h)$ enforces interface continuity between reinforcements and matrix regions, and will be defined in Section 2.4.

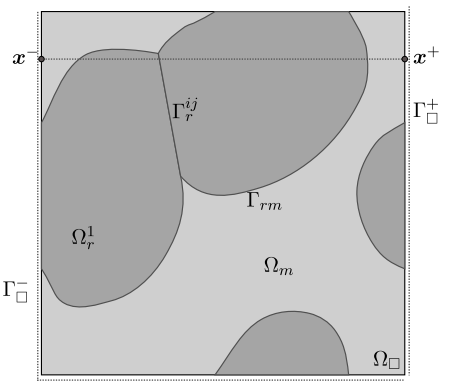

Fig. 1. A typical set-up for a meso-scale problem.

2.1. Discretisation of the bundle domain Ω_r

As the focus of this paper is on a discretisation method, we assume that the geometry for the fibre reinforcements Ω_r^i are readily available. With the geometric description of the bundles in-place, we follow IMM [30] and suggest to independently mesh the fibre bundle domains Ω_r^i with boundary-fitted elements that match that of Ω_r. Note that the fibre bundles are often relatively simple geometrical entities, consisting of interlaced cylindrical tubes, which makes the meshing procedure of these relatively simple. Moreover, as we choose to mesh the fibre bundles independently from each other, the meshing procedure is further simplified, as each bundle discretisation is free of constraints from adjacent bundles and/or narrow matrix regions.

The boundary-fitted mesh for the bundle discretisation is denoted $\mathcal{T}_h^r$, and in Fig. 2(a) we exemplify the discretisation using triangular elements. Note that Ω_r can also be discretised with NURBS (IGA) elements, which is demonstrated in Section 3. Finally, we also note that it is also possible to discretise the bundles with FCM, in order to obtain a fully immersed approach. This has been performed for other types of micro structures, e.g. foam-line structures in [33], however, has not been investigated in the current work.

2.2. Discretisation of the matrix domain Ω_m using the finite cell method

Following the methodology of FCM, the matrix domain is represented by a simple background mesh with equally sized elements. The background mesh is built up with higher order B-splines [31,34]. As such, the basis is constructed from a tensor product of 1-dimensional B-Splines, forming the n^d-dimensional B-spline functions B^p, where p is the order of the B-splines and n^d is the dimension of the problem (either 2 or 3). In this work we will restrict ourselves to second order B-splines ($p = 2$), for which we expect to benefit from the smoothness of the basis, without unnecessarily increasing the computational complexity associated with raising the spline order even further. The (Bézier) elements formed by these B-splines are denoted $\mathcal{T}_h^{\mathcal{A}}$, which is depicted in Fig. 2(b).

The background mesh $\mathcal{T}_h^{\mathcal{A}}$ can in general be significantly reduced, as the B-spline functions that are entirely within the domain Ω_r will not influence the displacement field of the matrix. The elimination process of unsupported B-spline functions is carried out by examining each element in the background mesh, to determine if it intersects with the discretised geometry ($\mathcal{T}_h^r$) of the fibre bundles. To determine if a background element is fully contained within a bundle, an inside–outside check of the faces of the element is performed. Should all of the faces of a Bézier element be completely inside Ω_r (i.e. completely outside Ω_m), both the Bézier element and the corresponding B-spline functions are discarded (unless they are still active in another element). The active mesh associated with the reference problem is depicted in Fig. 2(c), and is defined as:

$$\mathcal{T}_h = \{T \in \mathcal{T}_h^{\mathcal{A}} \mid T \cap \Omega_m \neq \emptyset\} \tag{3}$$

In the active mesh of the matrix domain, two types of elements can be identified, (i) trimmed (a.k.a cut) elements, and (ii) internal elements. Trimmed elements are defined by:

$$\mathcal{T}_h^{\text{trim}} = \{T \in \mathcal{T}_h \mid T \backslash \Omega_m \neq \emptyset\}, \tag{4}$$

which are both inside and outside the matrix domain. Internal elements are fully inside the matrix domain:

$$\mathcal{T}_h^{\text{in}} = \{T \in \mathcal{T}_h \mid T \subset \Omega_m\}. \tag{5}$$

Examples of elements that belong to these sets are depicted in Fig. 2(c) (T_1 and T_2). The elements that belong to $\mathcal{T}_h^{\text{in}}$ can be treated with standard quadrature schemes with regard to numerical volume integration. The trimmed elements that belong to $\mathcal{T}_h^{\text{trim}}$ on the other hand, require special quadrature schemes in order to respect the separate domains for matrix and bundles. This is described in the next subsection.

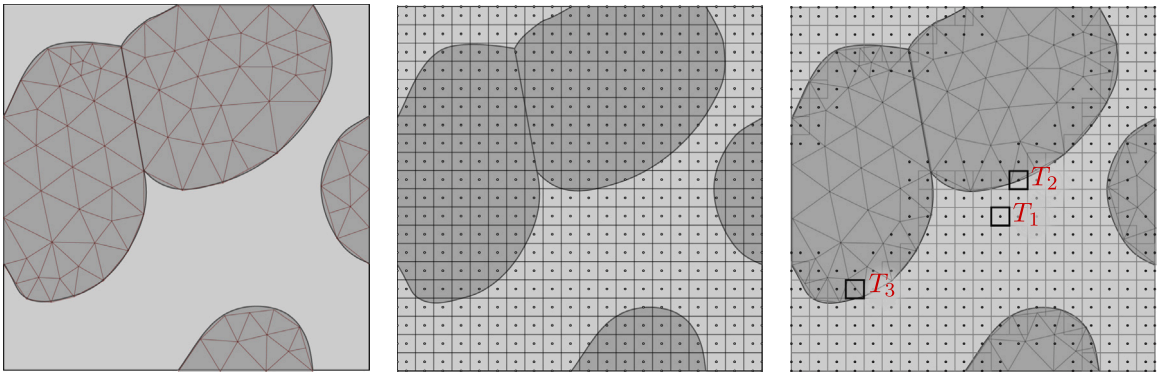

(a) Boundary fitted mesh $\mathcal{T}_h^r$. (b) Initial background mesh $\mathcal{T}_h^{\mathcal{A}}$. (c) Active background mesh $\mathcal{T}_h$.

Fig. 2. The matrix region is discretised with the FCM. Black dots • indicate control points of B-Spline mesh.

Remark. In order to determine if a background element lies inside or outside the boundary fitted mesh of Ω_r, a signed distance search (commonly used in contact algorithms) is performed to see if the element faces intersect any of the elements in $\mathcal{T}_h^r$. In order to make the inside–outside checks efficient, the adoption of efficient search algorithms is crucial. Here, we use the "bucket sort" algorithm, which is typically used for contact search algorithms [35]. □

2.3. Numerical integration of trimmed elements

The consideration of trimmed elements is a critical component of FCM, and has been studied extensively in the literature [36]. It is a necessity to construct specialised (numerical) integration schemes for the trimmed elements, which accurately respect the boundary of the matrix domain.

A prevalent strategy for devising integration schemes for trimmed elements in FCM involves employing multi-level subdivision through recursive bisection [37]. This approach is grounded in computational algorithms like quad-tree and oct-tree subdivision [38]. The method has found its popularity in that it is simple and robust regardless how the geometry cuts the trimmed elements [39,40].

The process of constructing specialised quadrature rules for each trimmed finite element is depicted in Fig. 3 (here exemplified with quad-trees). Denoting the trimmed finite element as a sub-cell at level $\varrho = 0$, the process involves subdividing the cell into four equally spaced cells (sub-cells), and to determine if any of the sub-cells intersects with Ω_r. If such an intersection is found, the subdivision process is repeated, but now at level $\varrho = 1$. This process is repeated recursively for each sub-cell, continuing until the process reaches the predefined maximum depth $\varrho_{\max}$.

After the subdivision process, each sub-cell in the oct-tree (or quad-tree) that intersects Ω_m, is assigned a numerical Gauss quadrature scheme. Here, we adopt the suggested "uniform degree lowering" approach for selection of the Gauss order at subsequent sub-cell levels, which was first suggested in [41], and further developed in [40]. In this strategy, the Gauss scheme order on sub-cell level $\varrho = 0$ is selected to integration degree $k_{\max}$, and then uniformly reduce the degree between two levels in such a way that the single point (degree zero) is reached at the levels $\varrho_{\max}$. For instance, with a depth of $\varrho_{\max} = 4$, and starting from a Gauss order $k_{\max} = 3$, the Gauss order for each sub-cell level is $(3, 2, 1, 0)$ (resulting in $(64, 27, 8, 1)$ points per sub-cell level in three dimensions). In this paper, we will use $k_{\max} = 3$, unless otherwise stated.

As a last step, an inside–outside check is performed for the quadrature points at the lowest subdivision level $\varrho = \varrho_{\max}$. If the quadrature point is inside the Ω_m (outside $\mathcal{T}_h^r$), it is included in the quadrature scheme; otherwise it is excluded.

2.4. Interface coupling

Since the discretisations of the matrix and the individual bundles within the model are decoupled, a method for interface coupling is needed. Here, we assume the matrix–bundle interface, Γ_{rm}, and adjacent bundle–bundle interfaces, Γ_r^{ij}, to be perfectly bonded, which is enforced using a penalty formulation. As such, the $a_h^r(\boldsymbol{u}_h, \boldsymbol{v}_h)$ and $a_h^{rm}(\boldsymbol{u}_h, \boldsymbol{v}_h)$ in Eq. (2) are defined as:

$$a_h^r(\boldsymbol{u}_h, \boldsymbol{v}_h) = \gamma_r \int_{\Gamma_r^{ij}} [\![\boldsymbol{u}_h]\!] \cdot [\![\boldsymbol{v}_h]\!] \, \mathrm{d}\Gamma, \quad a_h^{rm}(\boldsymbol{u}_h, \boldsymbol{v}_h) = \gamma_{rm} \int_{\Gamma_{rm}} [\![\boldsymbol{u}_h]\!] \cdot [\![\boldsymbol{v}_h]\!] \, \mathrm{d}\Gamma, \tag{6}$$

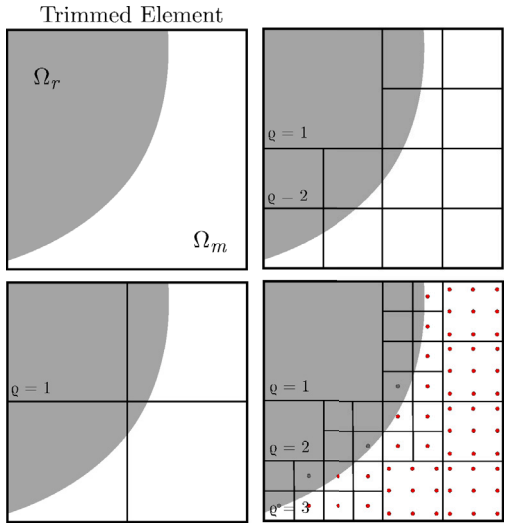

Fig. 3. Illustration of subdivision process with $\varrho_{\max} = 3$. Red dots are quadrature points.

where γ_{rm} and γ_r are penalty parameters for the respective interfaces. We note that another common alternative for interface coupling is the Nitsche's method [42], which is sometimes preferred for its variational consistency and stability without large penalty parameters. Despite its advantages, we have in the current work chosen the penalty method, as we are not interested in studying asymptotic convergence behaviour.

In the next subsections, we describe the process of obtaining the numerical integration rule required for evaluation of Eq. (6). The development of these interface integration schemes can be carried out as a pre-processing step.

Interface coupling between matrix and fibre bundles

As mentioned previously, the fibre bundles are discretised with boundary-fitted elements. As such, the boundary parametrisation of the bundles may conveniently be used for the interface integration for the bundle–matrix interface. The process is visualised in Fig. 4(a). First, a Gauss quadrature rule is established for each face of the boundary-fitted mesh that is part of Γ_{rm}. Next, Gauss quadrature points are defined on the face elements of the bundle mesh, which are then matched with corresponding parametric points in the elements of the FCM mesh. As such, all interface pairs (points and elements) are recorded and stored, and later used for the evaluation of the penalty constraint in Eq. (6).

Interface coupling between bundles

The construction of a numerical integration rule for adjacent bundles is visualised in Fig. 4(b). One side of the interface Γ_r^{ij} is chosen as the master side, and will act as the discretisation of the interface. Note that in general, due to approximations in the geometry generation, the surfaces meshes on either side of Γ_r^{ij} may be separated by a small distance. Therefore, when constructing the quadrature scheme for each of the interface elements on the master side, a minimum distance search for the closest point on the adjacent bundle must be performed. As for the matrix to bundle interface, these interface pairs are saved, and later used for the evaluation of the penalty constraint integral.

2.5. Stabilisation via ghost penalty method

In theory, the FCM procedure outlined in Sections 2.2 and 2.3 can be introduced and used in a conventional finite element setting. However, there are various challenges that may limit its practical viability. A significant challenge with immersed methods, such as FCM, relates to so-called *small cut problem* [43]. The *small cut problem* refers to that some trimmed elements can have arbitrarily small cuts, see e.g. element T_3 in Fig. 2(c). This negatively affects both the numerical stability (results are not drastically changed by small variations of the input) of the solution, and the condition number of the global (tangent) stiffness matrix. In fact, this limitation can render the previously mentioned weak formulation largely ineffective, especially for arbitrary mesh refinements, as the cut of the trimmed elements cannot be controlled.

There are different remedies proposed for controlling the *small cut problem*, e.g., α-stabilisation [44], element aggregation methods [43], or eigen-value stabilisation [45]. In the current contribution, we will use the approach known as the ghost-penalty method, first introduced by Burman et al. [46]. The ghost penalty method augments the weak form in Eq. (2) by an additional stabilisation term that acts on the faces of trimmed elements of the mesh. For problems considering linear elasticity, the ghost penalty term takes the form of:

$$g_h(\boldsymbol{u}_h, \boldsymbol{v}_h) = \gamma_g \sum_{F \in F_h} \sum_{k=1}^{p} h_F^{2k-1} \int_F [\![\partial_n^k \boldsymbol{u}_h]\!] \cdot [\![\partial_n^k \boldsymbol{v}_h]\!] d\Gamma. \tag{7}$$

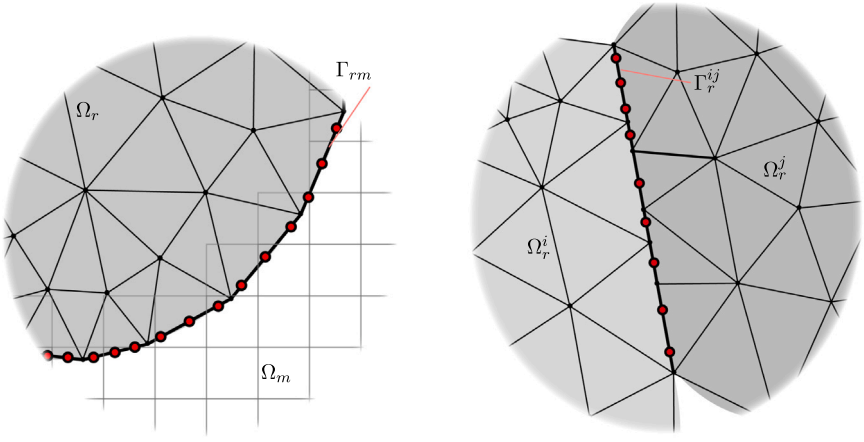

(a) Bundle to matrix (b) Bundle to bundle

Fig. 4. Visualisation of how to interface integration rules for the Γ_{rm} and Γ_r^{ij} is obtained. Red dots are quadrature points.

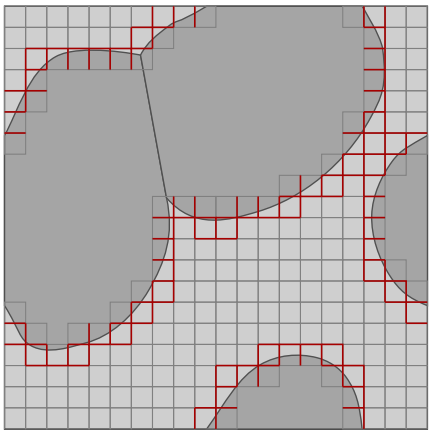

Fig. 5. Element faces belonging to the ghost interfaces $\mathcal{F}_h$.

Here, $\mathcal{F}_h$ is formally defined as the set of all interior faces that are shared by an element in $\mathcal{T}_h^{\text{trim}}$, and is illustrated in Fig. 5. Moreover, γ_g is a stability parameter term that needs to be chosen by the user, and h_F is the characteristic face length. Finally, ∂_n^k is the kth order face-normal derivative.

The ghost penalty term g_h terms penalises the differences in gradients across element boundaries, which greatly remedies both the stability of the solution and the conditioning number of the stiffness matrix for *small cut* elements. Determining a suitable value for γ_g is important, since if set too low, its role in stabilising the computations becomes negligible. Conversely, if it is too high, it will affect the accuracy of the results.

Remark. Since the background mesh used in this contribution is based on second order B-splines with C^1 continuity, the displacement jump and the gradient of the displacement is always equal to zero. As such, Eq. (7) can be reduced to only consider the Hessian of the normal displacement jump:

$$g_h(\boldsymbol{u}_h, \boldsymbol{v}_h) = \gamma_g \sum_{F \in \mathcal{F}_h} h_F^3 \int_F [\![\partial_n^2 \boldsymbol{u}_h]\!] \cdot [\![\partial_n^2 \boldsymbol{v}_h]\!] d\Gamma, \tag{8}$$

where the second order face normal gradient is computed as:

$$\partial_n^1 \boldsymbol{v} = (\boldsymbol{v} \otimes \boldsymbol{\nabla}) \cdot \boldsymbol{n}, \qquad \partial_n^2 \boldsymbol{v} = ((\boldsymbol{v} \otimes \boldsymbol{\nabla}) \otimes \boldsymbol{\nabla}) : (\boldsymbol{n} \otimes \boldsymbol{n}). \ \square \tag{9}$$

2.6. Note on selection of model parameters

In the modelling framework proposed in this paper, we introduce three parameters: the ghost parameter (γ_g), and the two penalty parameters for interface coupling between the matrix–bundle and bundle–bundle regions (γ_{rm} and γ_r, respectively). Determining suitable ranges for these parameters is crucial for the accuracy and stability of the model.

To identify appropriate values for these parameters for a specific meso-scale problem, we recommend conducting a parameter and sensitivity study for γ_g, γ_{rm}, and γ_r. This approach aims to ascertain a performance range for each parameter that ensures interface conditions are met satisfactorily (including the prevention of excessive interface separation) and that results are stabilised via the ghost parameter. If the meso-scale problem at hand is computationally intensive, making the parameter study time-consuming, we suggest building a simplified two-dimensional version of the problem, where the study can be conducted more quickly. Finally, when considering minor design variations (such as in geometric parameter studies), the penalty parameters can be kept fixed between variations.

3. Numerical examples of woven structures

In this section, we investigate the performance of the proposed modelling framework by means of three numerical examples. The first numerical example considers a two dimensional textile composite RVE, and illustrates the main techniques and features outlined in this paper. In the second numerical example, the immersed approach is used to estimate the homogenised membrane and bending stiffness for a 3D-woven composite. Finally, in the third example, we demonstrate how the proposed framework can be effectively used to study how the stress distribution in thin-ply woven composites are affected by the bundle thickness.

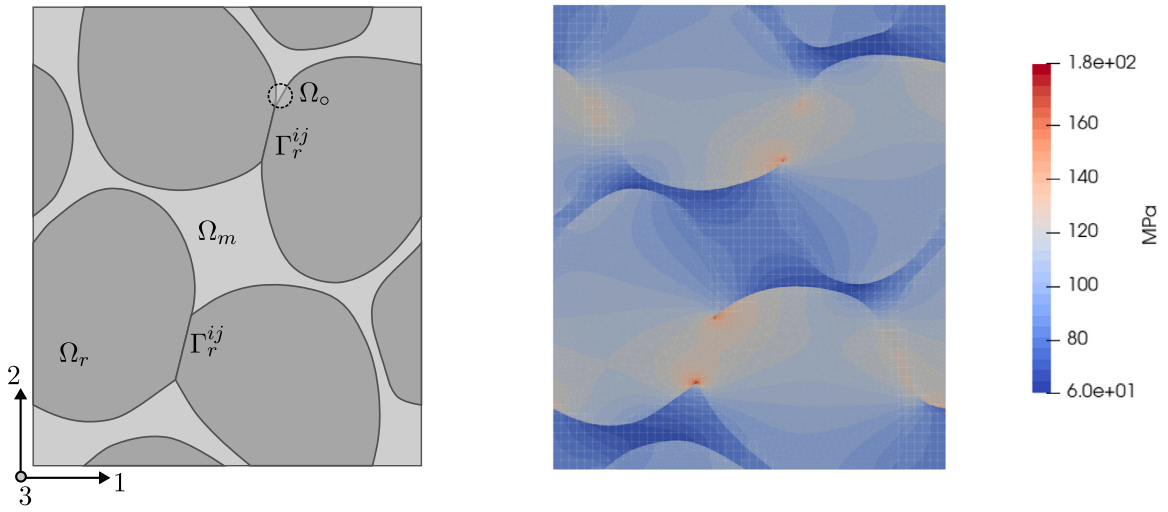

(a) Problem definition (b) Solution σ^e

Fig. 6. The 2D domain representing and overview of solution (50×50, $\varrho_{\max} = 6$).

3.1. Two dimensional example

In this numerical example, we illustrate the proposed modelling framework by analysing a fibre composite RVE in a two dimensional context. Our objective is to illustrate and assess how various model parameters, such as mesh-density, subdivision parameter $\varrho_{\max}$ and ghost penalty factor γ_g, influence the results. A periodic RVE representing the cross-section of a 3D woven composite will be used, which is illustrated in Fig. 6a (width $W = 2.18$ mm and height $H = 2.58$ mm). Note that this is a two-dimensional version of the problem in Section 3.2.

For the discretisation of the geometry, the fibre bundle domains are meshed using high fidelity second-order triangular elements. This mesh consists of approx. 8000 triangles and 17,000 nodes (average edge length 0.023 mm close to boundaries). Adjacent bundles are connected through penalty constraints. The pure matrix domain is represented using an FCM mesh, where the effect of the mesh-density of the background mesh and $\varrho_{\max}$ will be studied. As a reference solution, a high fidelity quadratic triangular mesh is used for the matrix and bundle phases. Note that in order to only study the effects of the FCM mesh, the same bundle mesh is used in both the immersed solution and reference solution. The full reference mesh contains approx. 15,000 triangles with 30,000 nodes (average edge length 0.0215 mm).

The fibre bundles of the RVE are modelled as transversely isotropic materials [47], with material parameters $E_L = 165$ GPa, $E_T = 9$ GPa, $G_{LT} = 5.6$ GPa, $\nu_{LT} = 0.34$ and $\nu_{TT} = 0.45$, where the fibre orientation is aligned with the out of plane direction (3-direction). The matrix region is modelled as a linear elastic material, with a Young's modulus $E = 3100$ MPa and Poisson's ratio $\nu = 0.35$. Moreover, plane strain is considered in both materials. The RVE is subjected to periodic displacement boundary conditions, with a uniaxial elongation of 1 percent in the x-direction: $[\![\boldsymbol{u}]\!]_\square = 0.01(x_1 - \bar{x}_1)\boldsymbol{e}_1$.

The parameters γ_g, γ_r and γ_{rm} are chosen through the strategy in Section 2.6. In this example, the parameters found most suitable for the problem are $\gamma_g = 100$ N/mm^2 and $\gamma_r = \gamma_{rm} = 9 \times 10^9$ N/mm^3.

3.1.1. Results

First, we investigate how the result converges with mesh refinement and subdivision depth ($\varrho_{\max}$) for the matrix phase. In regard to global convergence, e.g. average stiffness response, we merely note that the solution converges quickly regardless of the subdivision depth $\varrho_{\max}$ and for relatively low FCM mesh densities. However, such global convergence measures may not reveal what happens at local points, and in the following we therefore focus the convergence study to a local region of the mesh.

The local region studied is a circular area with a radius of $r = 5\,\mu$m, and is denoted $\Omega_\circ$ in Fig. 6a. This region was identified to be the most challenging area, as it situated in an area where two bundles meet. In this region, the maximum effective stress of the in-plane components, $\sigma^e = \sqrt{\sigma_{\alpha\beta}\sigma_{\alpha\beta}}, \alpha = \beta = 1, 2$ (visualised in Figure Fig. 6(b)), is monitored for each subdivision depth and each FCM discretisation.

In Fig. 7, the convergence of the maximum σ^e in the local region with respect to subdivision depth and FCM discretisations. It can be observed that the solution converges with respect to both quantities. For $\varrho_{\max}$, we note that it is important that a sufficiently high value for $\varrho_{\max}$ is chosen, otherwise the geometric features are not sufficiently captured, and artificial stresses anomalies (stress spikes) may occur. This is especially evident for $\varrho_{\max} = 2$, where the predicted stress values in $\Omega_\circ$ is greatly overestimated for all FCM discretisation. The issue is further illustrated in the images in Fig. 8, where to local region of interest is magnified. It can be seen that small stress spikes are present near the tip in Fig. 8(a), which are resolved for $\varrho_{\max} = 6$ Fig. 8(b).

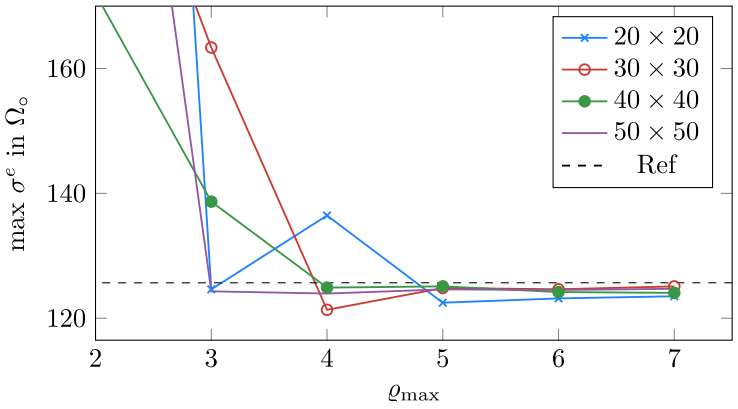

Fig. 7. Convergence of the peak stress in a localised region of the mesh.

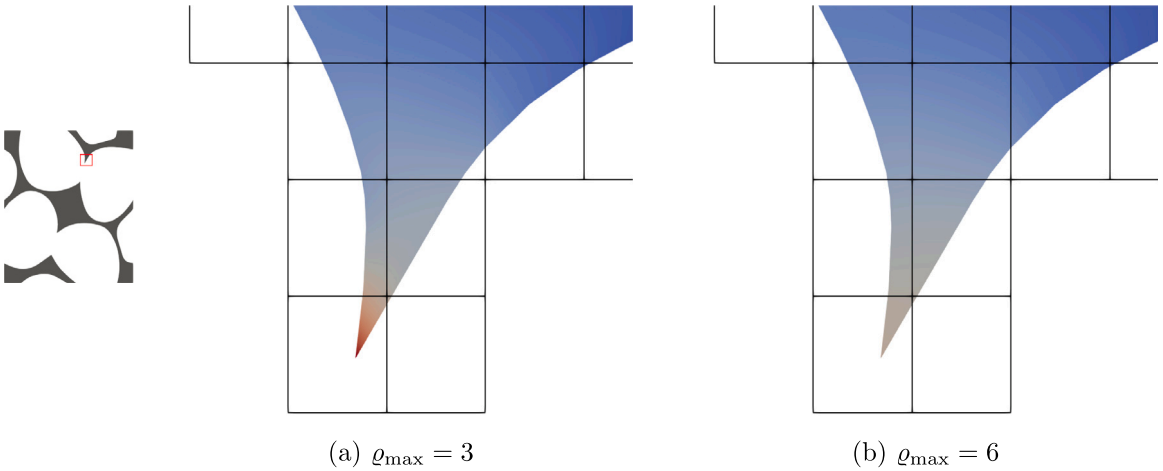

Fig. 8. σ^e for FCM mesh of 30 × 30 and different values of $\varrho_{\max}$. For low values of $\varrho_{\max}$, the geometry is not fully captured, and the stress in certain regions are poorly approximated.

For the convergence with respect to the mesh-density, it can be concluded that the maximum stress in the region converges for relatively coarse mesh-densities, due to the high accuracy in approximation resulting from the second order B-Splines.

Fig. 9 illustrates the importance of the stabilising properties of the ghost-penalty method γ_g. For low values of γ_g, stress spikes are observed in trimmed FCM elements with very low volume fractions (*small cut problem*). By using an appropriate value of $\gamma_g = 100$ N/mm^2, these stress spikes are mitigated. Note that the occurrence of the stress spikes is somewhat stochastic, and is influenced by factors such as the penalty-parameter, mesh-size and condition number of trimmed elements. Fig. 9 show the stresses for $\gamma_{rm} = 9{\times}10^6$ N/mm^3 (as the stress spikes did not appear for the current penalty parameter of $\gamma_{rm} = 9{\times}10^9$ N/mm^3). Indeed, the penalty constraints and the ghost penalty are similar in their weak forms, which indicates that the penalty constraints has some stabilising effects as well. It can be concluded that stabilisation by e.g. the ghost penalty method is important for robust simulations as elements with small low volume fractions (and bad condition numbers) will appear for arbitrary mesh refinements.

We also note that minor stress fluctuations, approximately at a magnitude of plus/minus 5 percent, can be identified at some locations in the bundles just next to interfaces between bundle and matrix regions. These stress fluctuations may be attributed to the application of the penalty interface law as outlined in previous research, cf. e.g. [48]. However, the stress fluctuations were not resolved by applying Nitsche's method, and since we believe that they are within acceptable engineering error tolerances, they are not further addressed in this paper. Additionally, we emphasise that such fluctuations also did not appear in the subsequent examples.

3.2. Stiffness and stress prediction in 3D woven composites

In the second example, we analyse the meso-scale structure of a 3D woven composite, focusing on the homogenised membrane and bending stiffnesses, but also demonstrating the stress distributions predicted by the immersed approach. The reinforcement of the 3D composite unit cell is depicted in Fig. 10(a) and comprises yarns in warp, horizontal weft, and vertical weft orientations,

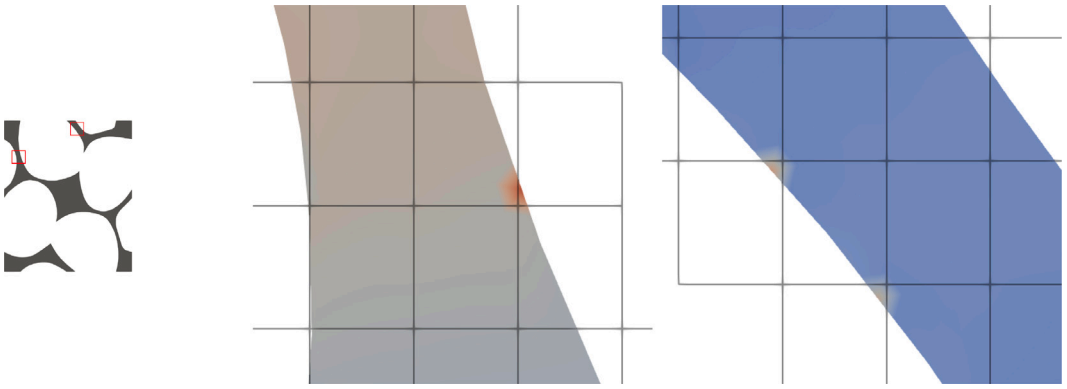

Fig. 9. σ^e for $\gamma_g \approx 0.0$ and $\gamma_{rm} = 9 \times 10^6$. Stress spikes for small-cut elements can be observed for low values of γ_g ($50 \times 50, \varrho_{\max} = 6$).

embedded within a polymer matrix. The unit cell geometry was initially developed in [49], with the methodology elaborated in [50]. The RVE model contains detailed information about the local fibre orientations along the bundles as well as locally varying fibre volume fractions within the bundles. Furthermore, a quadratic tetrahedral mesh for the total unit cell (both bundles and matrix) will serve as a reference for our FCM analysis (approx. 195,000 elements, 280,000 nodes, median edge length 0.118 mm).

The dimensions of the unit cell in the 1, 2 and 3 directions are $L_1 = 11.7$ mm and $L_2 = L_3 = 2.18$ mm. The yarn bundles are modelled as transversely isotropic. Due to the local variations in fibre volume fraction within each bundle, resulting from a varying bundle cross-sectional area, the elastic properties vary in the ranges $E_L = 100$–146 GPa, $E_T = 7$–10 GPa, $G_{LT} = 3$–5 GPa, $\nu_{LT} = 0.27$–0.30 and $\nu_{TT} = 0.40$–0.49. The volume between the bundles, being matrix pockets, are modelled as linear elastic with material parameters $E = 3100$ MPa and $\nu = 0.35$.

The homogenised membrane stiffness, $\overline{EA}$, and bending stiffness, $\overline{EI}$, are computed using homogenisation techniques for plates as described in [51]. For the homogenisation of membrane stiffness, we apply the periodic displacement boundary condition $[\![\boldsymbol{u}]\!]_\square = \bar{\varepsilon}_{11}[x_1 - \bar{x}_1]\boldsymbol{e}_1, \bar{\varepsilon}_{11} = 0.01$ on the lateral sides of unit-cell (top and bottom surfaces are free), and compute the stiffness as

$$\overline{EA} = \frac{1}{\bar{\varepsilon}_{11} L_1} \int_{\Omega_\square} \sigma_{11} \, \mathrm{d}\Omega. \tag{10}$$

Similarly, for the effective bending stiffness, we use the boundary condition $[\![\boldsymbol{u}]\!]_\square = x_3 \bar{\kappa}_{11}[x_1 - \bar{x}_1]\boldsymbol{e}_1, \bar{\kappa}_{11} = \frac{0.01}{0.5 L_3}$ m^{-1}, and compute the stiffness as

$$\overline{EI} = \frac{1}{\bar{\kappa}_{11} L_1} \int_{\Omega_\square} x_3 \sigma_{11} + \sigma_{13}(x_1 - \bar{x}_1) \, \mathrm{d}\Omega. \tag{11}$$

For the analysis, the bundles are discretised with a quadratic tetrahedral mesh (approx. 125,000 elements and 68,000 nodes (median element edge length 0.118 mm)). The matrix region is modelled with a FCM mesh, see Fig. 10(b), where the mesh-density and $\varrho_{\max}$ will be varied. Due to the large number of trimmed element in this problem, we set $k_{\max} = 2$ (three quadrature points in each direction), to limit the total amount of quadrature points. Finally, the model parameters are set to $\gamma_g = 100$ N/mm^2 and $\gamma_{rm} = 1.5 \times 10^6$ N/mm^3 (note that there exist no bundles that share an interface (Γ_r^{ij}) for the current RVE, and γ_r is therefore not used).

3.2.1. Results

The resulting membrane and bending stiffness, resulting from various FCM discretisations and subdivision depths $\varrho_{\max}$, are presented in Table 1. The homogenised stiffness from the reference solution predicts $\overline{EI} = 101,445$ Nmm^2 and $\overline{EA} = 307,532$ N. As expected, the homogenised stiffnesses predicted by the FCM method, both in bending and tension, agree with the reference solution, largely irrespectively of the FCM mesh size or subdivison depth. Thereby, it can be concluded that the subdivision algorithm effectively captures the correct volume fraction, even with relatively low values of $\varrho_{\max}$, as this is the most influential factor in the resulting stiffness predictions.

An overview of the bending-induced local distribution of the stress component σ_{11} in the matrix region is presented in Fig. 11 (stresses from FCM solution has been projected on the reference mesh for easy comparison). It can be observed that the immersed approach largely predicts the same overall distribution of the stress field as obtained by the reference finite element model.

3.3. Parameter study of woven spread tow composite

In this numerical analysis, we will investigate the meso-scale properties of plain 2D woven spread tows composites. The focus is on a parameter study to examine variations in stresses for different bundle thicknesses. The proposed immersed analysis approach

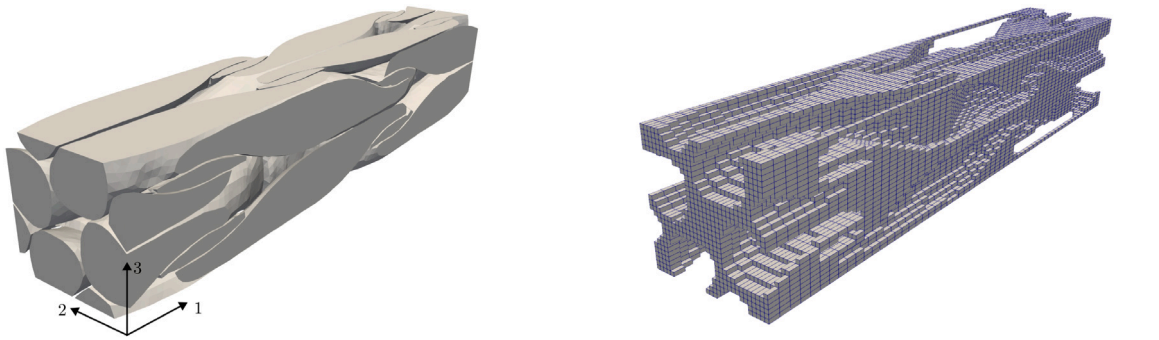

(a) The fibre reinforcements. (b) Computational FCM domain ($60 \times 30 \times 30$).

Fig. 10. The unit cell of a 3D woven composite.

Table 1
Homogenised bending and membrane stiffness, and number of quadrature points (in the FCM mesh) for various choices of discretisations and $\varrho_{\max}$.

	Bending $\overline{EI}$ [Nmm^2]	Membrane $\overline{EA}$ [N]	No. quadrature points
$40 \times 20 \times 20$			
$\varrho_{\max} = 2$	101,894	308,707	$0.28 \cdot 10^6$
$\varrho_{\max} = 3$	101,927	308,818	$1.1 \cdot 10^6$
$\varrho_{\max} = 4$	101,931	308,823	$3.7 \cdot 10^6$
$50 \times 25 \times 25$			
$\varrho_{\max} = 2$	101,639	308,124	$0.56 \cdot 10^6$
$\varrho_{\max} = 3$	101,636	308,128	$2.1 \cdot 10^6$
$\varrho_{\max} = 4$	101,637	308,129	$6.1 \cdot 10^6$
$60 \times 30 \times 30$			
$\varrho_{\max} = 2$	101,430	307,665	$0.91 \cdot 10^6$
$\varrho_{\max} = 3$	101,460	307,710	$3.2 \cdot 10^6$
$\varrho_{\max} = 4$	101,466	307,717	$9.0 \cdot 10^6$

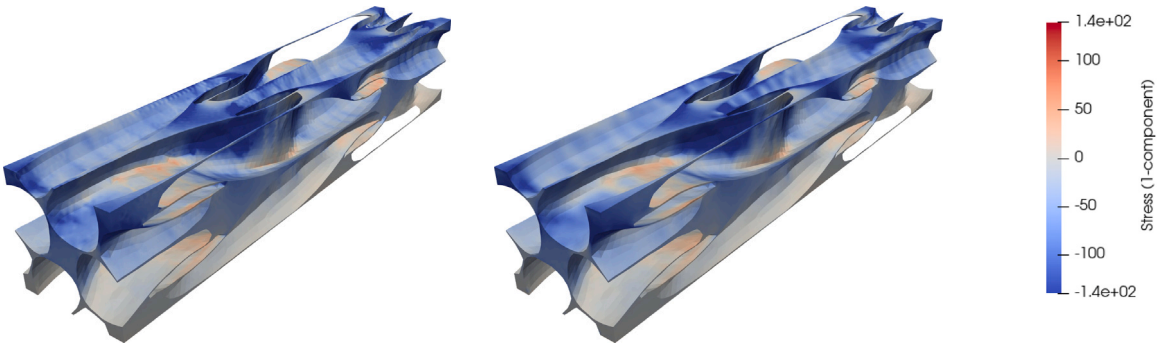

(a) Reference (FEM) (b) Immersed ($60 \times 30 \times 30$, $\varrho_{\max} = 4$)

Fig. 11. Stresses in 1-direction for the bending case.

is especially effective for these kinds of parameter studies, as it allows for streamlined discretisation of each unique geometry (with different thicknesses). This approach reduces the time and effort that would be required to generate traditional finite element meshes for each bundle thickness.

The geometry of the woven spread-tow is generated from a script, where the bundle geometry is parametrised with three parameters; the bundle width b, bundle thickness h, and the distance between adjacent bundles g, see Fig. 12. We employ second order B-Splines for geometrical description of the spread-tow geometry, enabling direct use in analysis without a separate meshing procedure of the bundles. For the current study, the bundle width $b = 7.0$ mm and the inter-bundle distance $g = 0.4$ mm are kept constant, while the bundle thickness h is varied between 0.05 mm to 0.2 mm.

As mentioned, the geometry of the bundles is represented by second order C^1 continuous B-Splines, which then are used directly for the bundle discretisation in the analysis. Each bundle has $38 \times 15 \times 3$ Bézier elements in the length, width and thickness

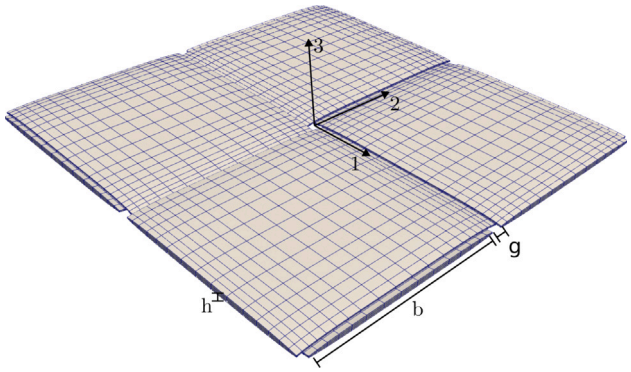

Fig. 12. Illustration of the geometry of the woven spread tows. The geometry in the figure has the dimensions $h = 0.2$ mm, $b = 7.0$ mm and $g = 0.4$ mm.

directions, respectively (elements shown in Fig. 12). The spread-tows will be immersed in a surrounding matrix material, which is modelled with an FCM mesh discretised with $51 \times 51 \times 11$ elements, with $\varrho_{\max} = 3$. The matrix domain is extended above and below the bundles to an amount corresponding to 10 percent of the bundle-thickness. This vertical extension of the matrix domain is done to avoid zero-volume elements at these locations. Moreover, the four interfaces where the bundles are in contact, are assumed to be perfectly bonded (which is enforced through the penalty method). In order to validate the results, we will use a reference solution with high fidelity quadratic tetrahedral elements (approx. 1,000,000 elements, 1,540,000 nodes, edge length 0.1 mm), for the case when the thickness is 0.2 mm.

The material of the matrix is set to simple linear elastic material with Young's modulus $E = 4$ GPa and Poisson's ratio $\nu = 0.35$. The material for the bundles is chosen to be transversely isotropic, with material parameters $E_L = 165$ GPa, $E_T = 9$ GPa, $G_{LT} = 5.6$ GPa, $\nu_{LT} = 0.34$ GPa and $\nu_{TT} = 0.45$, where the material direction follows the direction of the bundle geometry.

The spread-tow RVEs are subjected to uniaxial elongation of 1 percent in the x-direction, applied through periodic displacement boundary conditions along all boundaries of the RVE. This emulates that the layer is embedded inside a laminate where the boundary effect of the free surfaces on the top and bottom can be ignored.

For this study, it was found that a stability parameter γ_g of 100 N/mm^2 stabilised the results well, and that $\gamma_r = \gamma_{rm} = 165 \times 10^4$ N/mm^3 gave a good fulfilment of the interface constraints.

3.3.1. Results

The stresses are investigated along various lines at the mid-surface of the tows, with the objective to assess effects of the bundle thickness. Fig. 13 shows the variation of the transverse stress σ_T along two different bundles. It can be seen that the transverse stress increases close to the waviness, and that the effect is more pronounced for larger bundle thickness. This confirms that the reduced waviness resulting from thinner spread tows have a beneficial effect on the transverse stresses.

Fig. 14 shows the variation of the longitudinal stress component σ_L, where it can be seen that the thinner plies experience slightly larger stress values, but they are largely unaffected. The marginally larger longitudinal stress in the thinner plies can be explained by the fact that, for larger bundle thicknesses, more of the strain/deformation is concentrated at the weave/intersection. As such, when the undulation decreases for the thinner plies, the strain is more evenly distributed along the length of the bundle.

To summarise, the analysis indicates that the transverse stresses increase with greater bundle thickness. This finding demonstrates that enhanced toughness against matrix cracking is achieved with thinner plies, where transverse stresses significantly influence matrix cracking. It is important to note that this analysis does not consider the in-situ effect observed in thin spread tow composites, where matrix cracking in the transverse areas is further suppressed by the adjacent plies. This particular aspect of study has been explored in works such as Zrida et al. [52].

4. Conclusions

In this manuscript, we have explored the application of immersed methods for modelling fibre-reinforced meso-scale structures. The Finite Cell Method, in conjunction with second-order B-splines, is utilised to discretise the pure matrix regions of meso-scale structures, while the fibre bundles are discretised separately using boundary-fitted elements. Moreover, the bundles and matrix regions are coupled via penalty constraints. The framework offers a streamlined discretisation process that reduces the manual meshing effort typically necessary for discretising complex fibre composite meso-scale geometries.

The performance of the proposed immersed modelling framework is evaluated through three numerical examples. First, the method is demonstrated in a two-dimensional context, where the convergence of stresses is investigated with respect to the mesh density and subdivision parameter $\varrho_{\max}$. It is shown that the use of an appropriate stabilisation method, specifically, the ghost-penalty method, is important to obtain stable solutions, without nonphysical spikes and oscillations in the resulting stress field. Moreover, it is evident from this example that many subdivisions $\varrho_{\max}$ (and thereby quadrature points) are required to accurately predict the

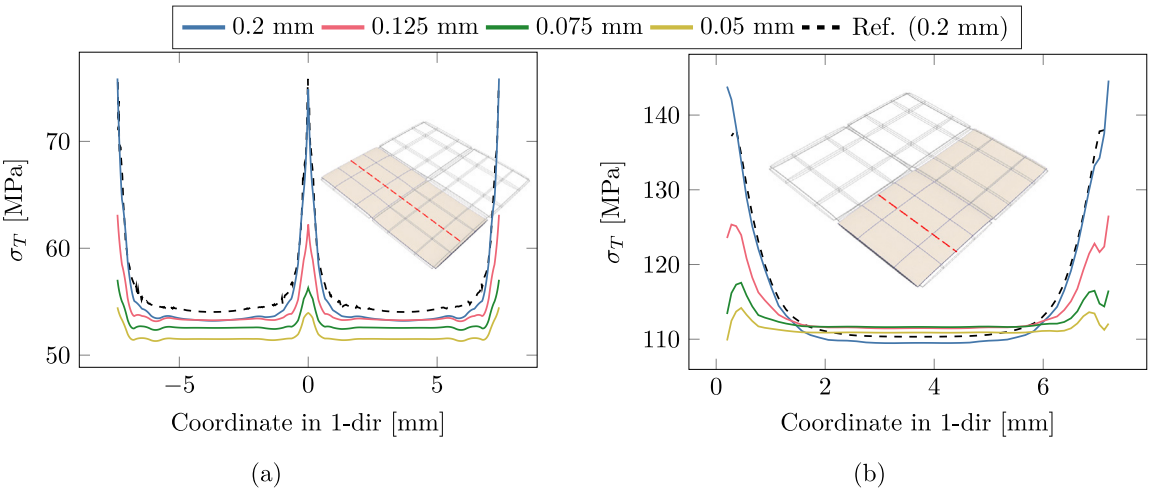

Fig. 13. Transverse stresses σ_T along the mid-surface of the bundles, indicated by the path of the dashed red line.

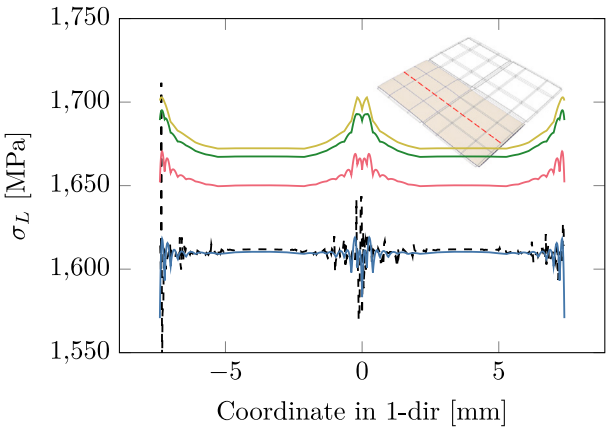

Fig. 14. Longitudinal stresses σ_L along the mid-surface of the bundles, indicated by the path of the dashed red line.

stresses in narrow areas between adjacent bundles. This is due to the fact that, for low values of $\varrho_{\max}$, the geometric features in these areas are not accurately captured. As a consequence, the stress prediction is affected negatively.

Next, the method is applied to a 3D-woven composite, for which the homogenised membrane and bending stiffness properties are calculated. It is demonstrated that the homogenised stiffness properties quickly converge with respect to FCM mesh density and subdivision parameter $\varrho_{\max}$, since the volume fraction is well captured by the method. Moreover, the stress values qualitatively show good agreement with the reference solution obtained with standard tetrahedral FE-mesh. Finally, in the third example, the immersed modelling framework is employed in a parameter study of thin-ply woven composites to investigate the influence of bundle thickness on resulting stresses. We show that the immersed modelling approach facilitates an efficient exploration of various bundle thicknesses, without the need for manual meshing of each configuration.

From the numerical examples, we draw the conclusions that the proposed modelling approach is a viable alternative for linear elastic simulations, e.g. for analysing stresses and strains, or predicting elastic stiffnesses. Compared to e.g. voxel-methods, the immersed modelling approach better predict stresses, without predicting erroneous stress peaks typically found in the step-like nature of voxel approaches. However, we note that the proposed method with FCM requires some manual intervention for the meshing of the bundles, while voxel methods are typically fully automatic.

Finally, as an outlook, the goal is to extend the framework to non-linear simulations, e.g., with non-linear material models in the matrix phase and interfaces. As an example, the interfaces between bundles, currently modelled as perfectly bonded with a penalty method, can be extended with non-linear cohesive zone laws. However, it is evident that the current approach of generating the quadrature scheme for trimmed elements results in a large number quadrature points. While this requirement is manageable for linear/static simulations, it will result in significant computational demands (both in terms of memory and processing speed) for non-linear simulations. As such, further research is required to ascertain how to adapt the framework for efficient analysis of non-linear problems. Here, more efficient methods for generating adaptive integration schemes, such as moment fitting, may be highly beneficial [53].

CRediT authorship contribution statement

Elias Börjesson: Writing – review & editing, Writing – original draft, Visualization, Validation, Methodology, Investigation, Formal analysis, Data curation, Conceptualization . **Clemens V. Verhoosel:** Writing – review & editing, Writing – original draft, Supervision, Funding acquisition, Methodology, Conceptualization. **Joris J.C. Remmers:** Writing – review & editing, Writing – original draft, Supervision, Funding acquisition, Methodology, Conceptualization. **Martin Fagerström:** Writing – review & editing, Writing – original draft, Supervision, Funding acquisition, Methodology, Conceptualization.

Declaration of competing interest

The authors declare that they have no known competing financial interests or personal relationships that could have appeared to influence the work reported in this paper.

Data availability

Data will be made available on request.

Declaration of Generative AI and AI-assisted technologies in the writing process

During the preparation of this work the author(s) used ChatGPT in order to enhance the manuscript's language. After using this tool/service, the author(s) reviewed and edited the content as needed and take(s) full responsibility for the content of the publication.

Acknowledgements

The work in this paper has been funded by the Swedish Research Council through grant no. 2018-05345. Financial support has in part also been provided by Vinnova's strategic innovation programme LIGHTer, Sweden (LIGHTer Academy grant no. 2020-04526). Moreover, the framework in this paper has been implemented in the Julia programming language [54], using the finite element toolbox Ferrite.jl [55] and tensor toolbox Tensors.jl [56].

Appendix A. Supplementary data

Supplementary material related to this article can be found online at https://doi.org/10.1016/j.finel.2024.104262.

References

[1] A. Arteiro, C. Furtado, G. Catalanotti, P. Linde, P. Camanho, Thin-ply polymer composite materials: A review, Composites A 132 (2020) 105777, http://dx.doi.org/10.1016/j.compositesa.2020.105777.
[2] F. Stig, S. Hallström, Assessment of the mechanical properties of a new 3D woven fibre composite material, Compos. Sci. Technol. 69 (11) (2009) 1686–1692, http://dx.doi.org/10.1016/j.compscitech.2008.04.047, Experimental Techniques and Design in Composite Materials (ETDCM8) with Regular Papers.
[3] A. Karimah, M.R. Ridho, S.S. Munawar, D.S. Adi, Ismadi, R. Damayanti, B. Subiyanto, W. Fatriasari, A. Fudholi, A review on natural fibers for development of eco-friendly bio-composite: characteristics, and utilizations, J. Mater. Res. Technol. 13 (2021) 2442–2458, http://dx.doi.org/10.1016/j.jmrt.2021.06.014.
[4] S.V. Lomov, D.S. Ivanov, I. Verpoest, M. Zako, T. Kurashiki, H. Nakai, S. Hirosawa, Meso-FE modelling of textile composites: Road map, data flow and algorithms, Compos. Sci. Technol. 67 (9) (2007) 1870–1891, http://dx.doi.org/10.1016/j.compscitech.2006.10.017.
[5] J. Ryatt, M. Ramulu, Numerical investigation of the application of voxel based meshes for stochastic tow based discontinuous composites, Finite Elem. Anal. Des. 214 (2023) 103874, http://dx.doi.org/10.1016/j.finel.2022.103874.
[6] C. Oddy, T. Ekermann, M. Ekh, M. Fagerström, S. Hallström, F. Stig, Predicting damage initiation in 3D fibre-reinforced composites – The case for strain-based criteria, Compos. Struct. 230 (2019) 111336, http://dx.doi.org/10.1016/j.compstruct.2019.111336.
[7] T. Wehrkamp-Richter, N.V. De Carvalho, S.T. Pinho, Predicting the non-linear mechanical response of triaxial braided composites, Composites A 114 (2018) 117–135, http://dx.doi.org/10.1016/j.compositesa.2018.08.011.
[8] A. Long, L. Brown, 8 - modelling the geometry of textile reinforcements for composites: TexGen, in: P. Boisse (Ed.), Composite Reinforcements for Optimum Performance, in: Woodhead Publishing Series in Composites Science and Engineering, Woodhead Publishing, 2011, pp. 239–264, http://dx.doi.org/10.1533/9780857093714.2.239.
[9] S. Lomov, WiseTex—A virtual textile composites software, in: Y. Kyosev, F. Boussu (Eds.), Advanced Weaving Technology, Springer International Publishing, Cham, 2022, pp. 293–318, http://dx.doi.org/10.1007/978-3-030-91515-5_7.
[10] B. Wintiba, B. Sonon, K.E.M. Kamel, T.J. Massart, An automated procedure for the generation and conformal discretization of 3D woven composites RVEs, Compos. Struct. 180 (2017) 955–971, http://dx.doi.org/10.1016/J.COMPSTRUCT.2017.08.010.
[11] F. Stig, S. Hallström, Spatial modelling of 3D-woven textiles, Compos. Struct. 94 (2012) 1495–1502, http://dx.doi.org/10.1016/J.COMPSTRUCT.2011.12.003.
[12] G. Zhou, X. Sun, Y. Wang, Multi-chain digital element analysis in textile mechanics, Compos. Sci. Technol. 64 (2004) 239–244, http://dx.doi.org/10.1016/S0266-3538(03)00258-6.
[13] S. Green, A. Long, B. El Said, S. Hallett, Numerical modelling of 3D woven preform deformations, Compos. Struct. 108 (2014) 747–756, http://dx.doi.org/10.1016/j.compstruct.2013.10.015.
[14] Y. Sinchuk, O. Shishkina, M. Gueguen, L. Signor, C. Nadot-Martin, H. Trumel, W. Van Paepegem, X-ray CT based multi-layer unit cell modeling of carbon fiber-reinforced textile composites: Segmentation, meshing and elastic property homogenization, Compos. Struct. 298 (2022) 116003, http://dx.doi.org/10.1016/j.compstruct.2022.116003.

[15] K.E.M. Kamel, B. Sonon, T.J. Massart, An integrated approach for the conformal discretization of complex inclusion-based microstructures, Comput. Mech. 64 (2019) 1049–1071, http://dx.doi.org/10.1007/S00466-019-01693-4/FIGURES/23.
[16] A. Li, K.E.M. Kamel, B. Wintiba, J.J. Remmers, M.G. Geers, T.J. Massart, A level set-based procedure for the cohesive modeling of yarn–yarn contacts in woven composite RVEs, Compos. Struct. 304 (2023) 116356, http://dx.doi.org/10.1016/J.COMPSTRUCT.2022.116356.
[17] H.J. Kim, C.C. Swan, Voxel-based meshing and unit-cell analysis of textile composites, Internat. J. Numer. Methods Engrg. 56 (7) (2003) 977–1006, http://dx.doi.org/10.1002/nme.594.
[18] Y.-T. Hwang, H.-J. Um, H.-S. Kim, Multi-scale progressive failure analysis of shear deformed woven fabric composites considering its pre-forming process, Composites A 174 (2023) 107713, http://dx.doi.org/10.1016/j.compositesa.2023.107713.
[19] S.D. Green, M.Y. Matveev, A.C. Long, D. Ivanov, S.R. Hallett, Mechanical modelling of 3D woven composites considering realistic unit cell geometry, Compos. Struct. 118 (2014) 284–293, http://dx.doi.org/10.1016/J.COMPSTRUCT.2014.07.005.
[20] Y. Cao, Y. Cai, Z. Zhao, P. Liu, L. Han, C. Zhang, Predicting the tensile and compressive failure behavior of angle-ply spread tow woven composites, Compos. Struct. 234 (2020) 111701, http://dx.doi.org/10.1016/J.COMPSTRUCT.2019.111701.
[21] Z. Li, D. Li, H. Zhu, Z. Guo, L. Jiang, Mechanical properties prediction of 3D angle-interlock woven composites by finite element modeling method, Mater. Today Commun. 22 (2020) 100769, http://dx.doi.org/10.1016/j.mtcomm.2019.100769.
[22] S. Yan, X. Zeng, A. Long, Meso-scale modelling of 3D woven composite T-joints with weave variations, Compos. Sci. Technol. 171 (2019) 171–179, http://dx.doi.org/10.1016/j.compscitech.2018.12.024.
[23] A. Doitrand, C. Fagiano, F.-X. Irisarri, M. Hirsekorn, Comparison between voxel and consistent meso-scale models of woven composites, Composites A 73 (2015) 143–154, http://dx.doi.org/10.1016/j.compositesa.2015.02.022.
[24] D. Schillinger, M. Ruess, The finite cell method: A review in the context of higher-order structural analysis of CAD and image-based geometric models, Arch. Comput. Methods Eng. 22 (2015) 391–455, http://dx.doi.org/10.1007/S11831-014-9115-Y/FIGURES/87.
[25] E. Burman, S. Claus, P. Hansbo, M.G. Larson, A. Massing, CutFEM: Discretizing geometry and partial differential equations, Internat. J. Numer. Methods Engrg. 104 (2015) 472–501, http://dx.doi.org/10.1002/NME.4823.
[26] S. Tabatabaei, S. Lomov, I. Verpoest, Assessment of embedded element technique in meso-FE modelling of fibre reinforced composites, Compos. Struct. 107 (2014) 436–446, http://dx.doi.org/10.1016/j.compstruct.2013.08.020.
[27] A. Düster, J. Parvizian, Z. Yang, E. Rank, The finite cell method for three-dimensional problems of solid mechanics, Comput. Methods Appl. Mech. Engrg. 197 (45) (2008) 3768–3782, http://dx.doi.org/10.1016/j.cma.2008.02.036.
[28] C.V. Verhoosel, E. Harald van Brummelen, S.C. Divi, F. de Prenter, Scan-based immersed isogeometric flow analysis, in: Frontiers in Computational Fluid-Structure Interaction and Flow Simulation: Research from Lead Investigators under Forty - 2023, Springer International Publishing, Cham, 2023, pp. 477–512, http://dx.doi.org/10.1007/978-3-031-36942-1_14.
[29] E.V. Iarve, D.H. Mollenhauer, E.G. Zhou, T. Breitzman, T.J. Whitney, Independent mesh method-based prediction of local and volume average fields in textile composites, Composites A 40 (2009) 1880–1890, http://dx.doi.org/10.1016/J.COMPOSITESA.2009.04.034.
[30] H.K. Adluru, E. Zhou, K.H. Hoos, C. Popelar, M.K. Ballard, D. Mollenhauer, D. Riha, A.S. Selvarathinam, E.V. Iarve, Performance prediction of interlock woven composites by independent mesh method, Composites A 165 (2023) 107317, http://dx.doi.org/10.1016/J.COMPOSITESA.2022.107317.
[31] D. Schillinger, E. Rank, An unfitted hp-adaptive finite element method based on hierarchical B-splines for interface problems of complex geometry, Comput. Methods Appl. Mech. Engrg. 200 (47) (2011) 3358–3380, http://dx.doi.org/10.1016/j.cma.2011.08.002.
[32] C. Verhoosel, G. van Zwieten, B. van Rietbergen, R. de Borst, Image-based goal-oriented adaptive isogeometric analysis with application to the micro-mechanical modeling of trabecular bone, Comput. Methods Appl. Mech. Engrg. 284 (2015) 138–164, http://dx.doi.org/10.1016/j.cma.2014.07.009, Isogeometric Analysis Special Issue.
[33] L. Radtke, P. Marter, F. Duvigneau, S. Eisenträger, D. Juhre, A. Düster, Vibroacoustic simulations of acoustic damping materials using a fictitious domain approach, J. Sound Vib. 568 (2024) 118058, http://dx.doi.org/10.1016/j.jsv.2023.118058.
[34] E. Rank, M. Ruess, S. Kollmannsberger, D. Schillinger, A. Düster, Geometric modeling, isogeometric analysis and the finite cell method, Comput. Methods Appl. Mech. Engrg. 249–252 (2012) 104–115, http://dx.doi.org/10.1016/j.cma.2012.05.022, Higher Order Finite Element and Isogeometric Methods.
[35] M.W. Heinstein, S.W. Attaway, J.W. Swegle, F.J. Mello, A general-purpose contact detection algorithm for nonlinear structural analysis codes, 1993, http://dx.doi.org/10.2172/10175733.
[36] A. Abedian, J. Parvizian, A. D"uster, H. Khademyzadeh, E. Rank, Performance of different integration schemes in facing discontinuities in the finite cell method, Int. J. Comput. Methods 10 (03) (2013) 1350002, http://dx.doi.org/10.1142/S0219876213500023.
[37] D. Schillinger, M. Ruess, N. Zander, Y. Bazilevs, A. Düster, R. Ernst, Small and large deformation analysis with the p- and B-spline versions of the finite cell method, Comput. Mech. (2012) 445–478, http://dx.doi.org/10.1007/s00466-012-0684-z.
[38] H. Samet, The Design and Analysis of Spatial Data Structures, Vol. 85, Addison-wesley Reading, MA, 1990.
[39] M. Petö, F. Duvigneau, S. Eisenträger, Enhanced numerical integration scheme based on image-compression techniques: application to fictitious domain methods, Adv. Model. Simul. Eng. Sci. 7 (1) (2020) http://dx.doi.org/10.1186/s40323-020-00157-2.
[40] S.C. Divi, C.V. Verhoosel, F. Auricchio, A. Reali, E.H. van Brummelen, Error-estimate-based adaptive integration for immersed isogeometric analysis, Comput. Math. Appl. 80 (11) (2020) 2481–2516, http://dx.doi.org/10.1016/j.camwa.2020.03.026, High-Order Finite Element and Isogeometric Methods 2019.
[41] A. Abedian, J. Parvizian, A. Düster, E. Rank, The finite cell method for the J2 flow theory of plasticity, Finite Elem. Anal. Des. 69 (2013) 37–47, http://dx.doi.org/10.1016/j.finel.2013.01.006.
[42] P. Hansbo, M.G. Larson, K. Larsson, Cut finite element methods for linear elasticity problems, Lect. Notes Comput. Sci. Eng. 121 (2017) 25–63, http://dx.doi.org/10.1007/978-3-319-71431-8_2/FIGURES/24.
[43] F. de Prenter, C.V. Verhoosel, E.H. van Brummelen, M.G. Larson, S. Badia, Stability and conditioning of immersed finite element methods: Analysis and remedies, Arch. Comput. Methods Eng. 30 (2023) 3617–3656, http://dx.doi.org/10.1007/S11831-023-09913-0/FIGURES/9.
[44] J. Parvizian, A. Düster, E. Rank, Finite cell method: h- and p-extension for embedded domain problems in solid mechanics, Comput. Mech. 41 (1) (2007) 121–133, http://dx.doi.org/10.1007/s00466-007-0173-y.
[45] G. Wadhah, U. Khuldoon, D. Alexander, An eigenvalue stabilization technique to increase the robustness of the finite cell method for finite strain problems, Comput. Mech. 69 (2022) 1225–1240, http://dx.doi.org/10.1007/s00466-022-02140-7.
[46] E. Burman, P. Hansbo, Fictitious domain finite element methods using cut elements: II. A stabilized Nitsche method, Appl. Numer. Math. 62 (4) (2012) 328–341, http://dx.doi.org/10.1016/j.apnum.2011.01.008.
[47] R.M. Jones, Mechanics of Composite Materials, second ed., Taylor and Francis Group, 2015.
[48] E. Svenning, A weak penalty formulation remedying traction oscillations in interface elements, Comput. Methods Appl. Mech. Engrg. 310 (2016) 460–474, http://dx.doi.org/10.1016/j.cma.2016.07.031.
[49] F. Stig, S. Hallström, A modelling framework for composites containing 3D reinforcement, Compos. Struct. 94 (9) (2012) 2895–2901, http://dx.doi.org/10.1016/j.compstruct.2012.03.009.
[50] F. Stig, S. Hallström, Spatial modelling of 3D-woven textiles, Compos. Struct. 94 (5) (2012) 1495–1502, http://dx.doi.org/10.1016/j.compstruct.2011.12.003.

[51] E. Börjesson, F. Larsson, K. Runesson, J.J. Remmers, M. Fagerström, Variationally consistent homogenisation of plates, Comput. Methods Appl. Mech. Engrg. 413 (2023) 116094, http://dx.doi.org/10.1016/j.cma.2023.116094.
[52] H. Zrida, M. Fagerström, Mesoscale modeling of ultra-thin woven fabric composite subjected to in-plane loading, Adv. Compos. Mater. (2022) http://dx.doi.org/10.1080/09243046.2022.2084983.
[53] S. Hubrich, P. Di Stolfo, L. Kudela, S. Kollmannsberger, E. Rank, A. Schröder, A. Düster, Numerical integration of discontinuous functions: moment fitting and smart octree, Comput. Mech. 60 (5) (2017) 863–881, http://dx.doi.org/10.1007/s00466-017-1441-0, URL http://dx.doi.org/10.1007/s00466-017-1441-0.
[54] J. Bezanson, A. Edelman, S. Karpinski, V.B. Shah, Julia: A fresh approach to numerical computing, SIAM Rev. 59 (1) (2017) 65–98.
[55] K. Carlsson, F. Ekre, Contributors, Ferrite.jl - Finite element toolbox for Julia, 2021, URL https://github.com/Ferrite-FEM/Ferrite.jl.
[56] K. Carlsson, F. Ekre, Tensors.jl — Tensor computations in Julia, J. Open Res. Softw. (2019) http://dx.doi.org/10.5334/jors.182.